Chinese Chemical Letters 34 (2023) 107853

Contents lists available at ScienceDirect

Chinese Chemical Letters

journal homepage: www.elsevier.com/locate/cclet

Dual-targeted nanoformulation with Janus structure for synergistic enhancement of sonodynamic therapy and chemotherapy

Zhifang Wang, Man Wang, Yanrong Qian, Yulin Xie, Qianqian Sun*, Minghong Gao, Chunxia Li*

Institute of Molecular Sciences and Engineering, Institute of Frontier and Interdisciplinary Science, Shandong University, Qingdao 266237, China

ARTICLE INFO

Article history:
Received 15 August 2022
Revised 7 September 2022
Accepted 22 September 2022
Available online 17 October 2022

Keywords:
Ultra-small
Janus structure
Mitochondrial targeting
CD44 targeting
Synergistic therapy
MR imaging

ABSTRACT

The accurate delivery of nanoparticles and organic small molecule drugs remains a serious challenge in nanoparticle-based tumor therapy. Dual-targeted therapy combining tumor cell targeting and organelle targeting is an effective solution. Here, an anticancer nanoformulation accurate delivery system was prepared using hyaluronic acid (HA) targeting CD44 receptors on the surface of tumor cells and IR780 iodine (IR780) targeting mitochondrial for delivery. The system is based on an ultra-small Janus structured inorganic sensitizer TiO_{2-x}@$NaGdF_4$ nanoparticles (TN NPs) prepared by one-step pyrolysis, further loaded with organic small molecule acoustic sensitizer IR780 and mitochondrial hexokinase II inhibitor lonidamine (LND), followed by encapsulation of HA. Ultra-small size nanoparticles exhibit strong tissue penetration, tumor inhibition and *in vivo* metabolism. Under ultrasound radiation, TN NPs and IR780 could produce a synergistic effect, effectively increased the efficiency of reactive oxygen species (ROS) production. Meanwhile, the released IR780 could smoothly target the mitochondria, and the ROS produced by IR780 can destroy the mitochondrial structure and disrupt the mitochondrial respiration. LND could inhibit the energy metabolism of tumor cells by reducing the activity of hexokinase II (HK II), which further accelerates the process of apoptosis. Furthermore, since the Janus structure allows the integration of multifunctional components into a single system, TN NPs can not only serve as an acoustic sensitizer to generate ROS, but the Gd element contained can also act as the nuclear magnetic resonance (MR) imaging contrast agent, suggesting that the nanoformulation can enable imaging-guided diagnosis and therapy. In conclusion, a new scheme to enhance sonodynamic therapy (SDT) and chemotherapy synergistically is proposed here based on ultra-small dual-targeted nanoformulation with Janus structure in the ultrasound radiation environment.

As a promising form of cancer treatment, SDT is based on ultrasound (US) triggered acoustic sensitizers that induce an excess production of ROS, resulting in various anti-tumor effects [1–4]. Recently, a number of inorganic acoustic sensitizers (*e.g.*, porphyrins, TiO_2, Bi_2MoO_6 and $MnWO_X$) [5–9] and organic small molecule acoustic sensitizers (*e.g.*, HMME, PpIX, Ce6 and IR780) [10–13] have been developed with impressive therapeutic results. TiO_2 has been well studied due to the capacity to generate ROS and the high chemical stability [14,15]. However, traditional TiO_2 nanoparticles typically display low efficiency of ROS generation due to their wide band gap (~3.20 eV) and the rapid recombination of electrons (e^-) and holes (h^+) in the energy band structure [16]. Recently, some groups have started to solve this problem through various strategies, such as forming oxygen-deficient layers on the TiO_2 surface [17], combining TiO_2 nanoparticles with other noble metals (*e.g.*, Pt, Fe, Au) [18–20] and compounding with semiconductors [21]. Particularly, TiO_{2-x} with an excellent oxygen-deficient layer has attracted our attention [22]. Unfortunately, in tumor therapy, in addition to the effect of nanoparticles, the therapeutic effect was limited by the accumulation and intracellular localization of nanoparticles at the tumor site, while the long-term accumulation also posed a significant health risk at the tumor site [23–26]. Therefore, it was important for us to improve the metabolism of nanoparticles *in vivo* while enhancing the accumulation and intracellular distribution of nanoparticles at the tumor site.

In order to prolong the circulation time of nanoparticles in the blood and enhance the accumulation at tumor sites, various drug delivery systems based on surface-coupled organic material strategies have been developed and widely used in cancer therapy [27–30]. Among them, HA has good biocompatibility and

* Corresponding authors.
E-mail addresses: sunqianqian@sdu.edu.cn (Q. Sun), cxli@sdu.edu.cn (C. Li).

https://doi.org/10.1016/j.cclet.2022.107853
1001-8417/

biodegradability, and can bind to CD44 receptors overexpressed on the surface of tumor cells, which is commonly used in various drug delivery systems in tumor therapy [31–33]. After entering the tumor microenvironment, HA-based encapsulated nanocomposites can be easily internalized through CD44 receptor-mediated recognition [34–36]. During the process of endocytosis, HYAL-2 (one type of hyaluronidases) initiates hydrolysis, degrading HA into fragments of approximately 20 kDa. The fragments then enter the lysosome and are further degraded by HYAL-1 (another type of hyaluronidases), ensuring the rapid release of the HA-encapsulated nanodrug into the tumor cytoplasm for action [37–39]. In addition to the strategy of targeting tumor cells, the development of nanoformulations with organelle targets is also of great significance [40–42]. Specifically, mitochondria have been implicated in cellular respiration as energy converters and have served as intracellular "engines" and "power plants". As research has shown, mitochondria are important organelles in cancer cells that undergo metabolic reprogramming. The number, structure and function of mitochondria are changed differently compared to normal cells to accommodate the rapid growth and reproduction of cancer cells [43–45]. Therefore, mitochondria-targeted approaches were considered to be an effective cancer treatment. IR780, as a near-infrared heptamethyl anthocyanin dye, has a strong affinity for tumor mitochondria and can be preferentially retained in the mitochondria [46,47]. Under the stimulation of applied ultrasound, IR780 can act as an acoustic sensitizer [48], generating significant amounts of ROS and inducing apoptosis [49,50]. LND, a potent inhibitor of glycolysis, not only reduced energy metabolism in tumor cells by inhibiting hexokinase II (HK II) activity, but also disrupted mitochondrial structure and interrupted cell respiration [51–53]. In addition to intercepting the energy supply of cancer cells, the immune system would also be more effectively regulated for cancer treatment. Therefore, we propose the hypothesis that IR780 utilized as an oxidative stress regulator to induce mitochondrial dysfunction by generating large amounts of ROS to synergize with LND and accelerate the apoptotic process of tumor cells.

Small size nanoparticles also have a significant impact in increasing the tumor penetration, cellular internalization and *in vivo* excretion of nanomaterials [54]. Studies have shown that, on the one hand, ultra-small nanoparticles could achieve deep penetration into the tumor tissue without modification, increasing the ability of nanoparticles to accumulate at the tumor site; on the other hand, ultra-small nanoparticles could be easily removed over a period of time and reduce the side effects of nanomaterials [55–57]. For a long time, the preparation of ultra-small Janus particles has been an important research direction and a difficult direction in materials science. Such asymmetric nanoparticles typically consist of several functional compartments, which allow for the integration of multi-functional components into a single system and expands the value of application in tumor therapy [58–61]. Therefore, ultra-small nanoparticles with Janus structure not only have excellent combined therapeutic or diagnostic effects, but also have inherent advantages in terms of *in vivo* metabolism and clearance.

Based on the above background, ultra-small Janus composite nanoparticles integrating SDT, cellular energy supply inhibition and dual-targeting function of tumor cells/cellular organelles may be a very promising strategy for cancer therapy. In our design, ultra-small TN NPs with Janus structure were synthesized in one step by improving the thermal decomposition strategy (Scheme 1A) [62]. Then, a TiO_{2-x}@$NaGdF_4$@IR780@LND-HA (TNILH) nanoplatform was

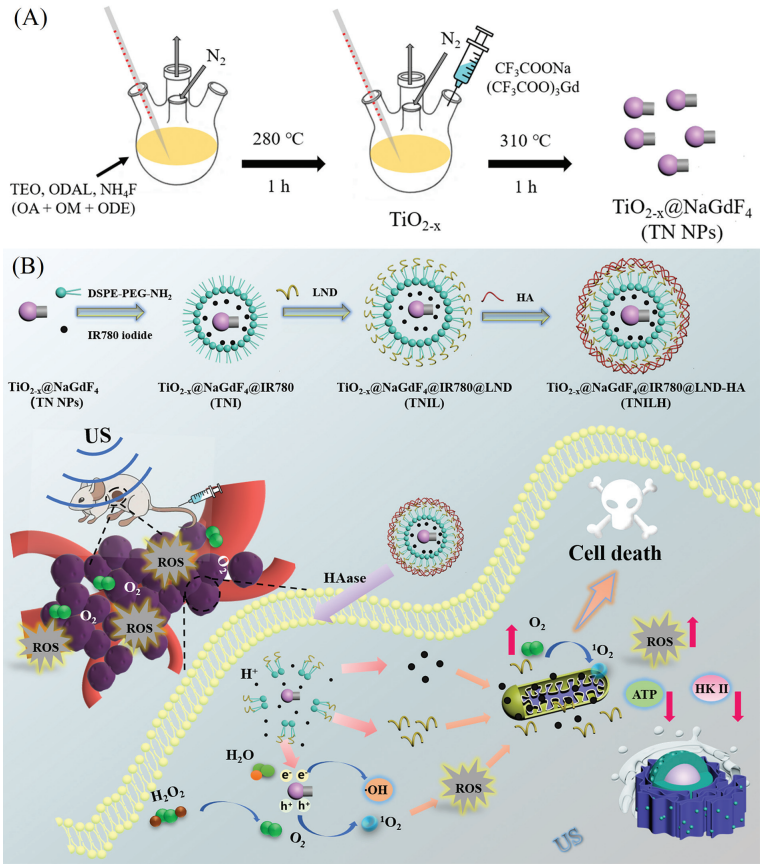

Scheme 1. Schematic diagram of material synthesis and anti-tumor mechanism. (A) Synthesis method of ultra-small TN NPs. (B) Schematic diagram of the synergistic multimodal antitumor therapy of TNILH.

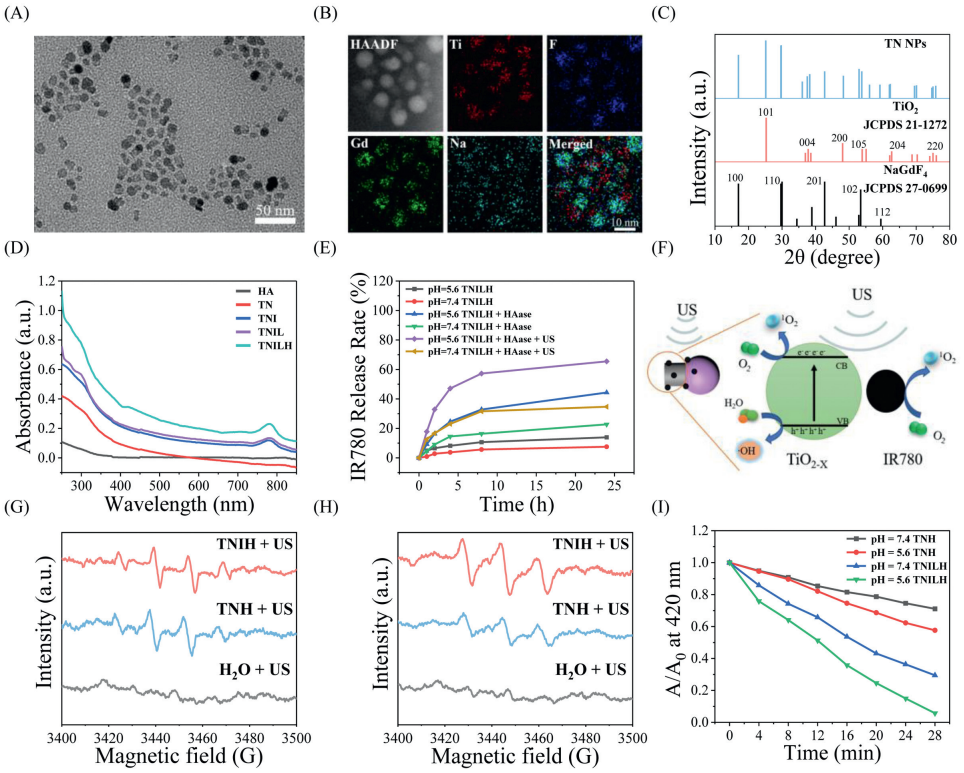

Fig. 1. Characterization of TNILH nanoformulation. (A) TEM image of TN NPs. (B) HAADF-STEM and elemental mapping images of TN NP. (C) XRD spectra. (D) UV-vis spectra of HA, TN, TNI, TNIL and TNILH. (E) Release rate of IR780 of TNILH dispersed in different conditions. (F) Mechanistic diagram of the synergistic effect of TN NPs and IR780 to enhance the efficiency of ROS production. (G) ESR spectra indicating $^{\bullet}OH$ generation by US-activated TNH and TNIH. (H) ESR spectra indicating $^{1}O_2$ generation by US-activated TNH and TNIH. (I) The change of absorption intensity of DPBF in different solutions under ultrasound radiation.

constructed by loading IR780, LND and surface-coated HA. Upon targeting of CD44 to tumor cells, hyaluronic acid was decomposed by HAase overexpressed in the tumor microenvironment, leading to the reduction in particle size and the increase in charge of the TNILH nanoformulation, which increases the endocytosis effect of tumor cells. IR780 can act as an acoustic sensitizer and synergize with TN NPs to improve ROS production efficiency and enhance SDT effect; when released in the acidic tumor microenvironment, IR780 can target mitochondria and synergize with hexokinase II inhibitor LND to induce mitochondrial damage and dysfunction and enhance the destructive effect on tumor tissues (Scheme 1B). It is worth mentioning that the Janus structure of TN NPs not only endows this nanoplatform with SDT functions, but also with MR imaging properties due to the presence of Gd elements, allowing real-time tracking of this nanoformulation for imaging-guided tumor synergistic therapy [63–65]. In addition, pharmacokinetic analysis demonstrated that the nanoformulation has a good *in vitro* efflux effect.

The synthesis steps were shown in Scheme 1A. Homogeneous and stable TN NPs were synthesized by thermal decomposition by adding titanium(IV) ethoxide, 1-octadecanol and ammonium fluoride (NH_4F) to the mixture of oleylamine, oleic acid and 1-octadecene, and after reacting at 280 °C for 1 h, the temperature was continued to 310 °C. Then rare earth precursors were added to the reaction system by direct injection, and the reaction was maintained for 1 h to obtain ultra-small and homogeneous TN NPs. Transmission electron microscopy (TEM) showed that the TN NPs had a Janus structure, with a length diameter of 12.74 nm, and had good monodispersity and homogeneity (Fig. 1A). High-angle annular dark-field scanning transmission electron microscopy (HAADF-STEM) and energy dispersive spectroscopy (EDS) elemental mapping images showed that the elements of Gd, Na and F were uniformly distributed in the same site, and the elements of Ti was distributed in another region (Fig. 1B). It further validated the successful synthesis of asymmetric TN NPs. X-ray diffraction (XRD) patterns of TN NPs showing typical diffraction peaks at 17.34°, 29.75°, 42.44°, 52.01° and 59.17° which were associated with the (100), (200), (201), (102) and (102) planes of the face-centered cubic phase of $NaGdF_4$, respectively; typical diffraction peaks at 25.40°, 37.52°, 48.29°, 52.94°, 63.08°, 70.10° and 75.29° were associated with the (101), (004), (200), (105), (204), (215) and (220) planes of the face-cantered cubic phase of TiO_{2-x} (Fig. 1C).

Polyethylene glycolized DSPE has excellent amphiphilic properties and has superior advantages in the encapsulation and delivery of molecules [66–68]. We chose to use DSPE-PEG-NH_2 polymer as the hydrophilic modification of TN NPs having the oleic acid hydrophobic layer on the surface, while hydrophilic layer between TN NPs and PEG can be used to adsorb the acoustically sensitive drug molecule IR780 in a non-covalent bonding manner. The before-and-after control picture of modified TN NPs by DSPE-PEG-NH_2 was shown in Fig. S1 (Supporting information). Then the nanoformulation were synthesized by activating the carboxyl groups of LND and HA and bonded to the amino end of PEG by amide bonding. The change in zeta potential and average hydrodynamic diameter of the different materials confirmed the successful performance of each synthesis step (Fig. S2 in Supporting information). Furthermore, the change of hydrodynamic diameters and zeta potential values indicated that the modified TNILH nanoformulation can be stabilized (Fig. S3 in Supporting information). The prepared TiO_{2-x}@$NaGdF_4$@DSPE-PEG-NH_2 (TN), TiO_{2-x}@$NaGdF_4$@IR780 (TNI), TiO_{2-x}@$NaGdF_4$@IR780@LND (TNIL) and TNILH nanoformulations showed excellent stability in phosphate buffered saline (PBS) and Dulbecco's Modified Eagle Medium (DMEM) containing 10% fetal bovine serum (Fig. S4 in Supporting information), and the non-

hemolytic effect of TNILH on erythrocytes provided the possibility of further *in vivo* application (Fig. S5 in Supporting information).

Further characterization was carried out by UV-vis spectroscopy. As shown in Fig. 1D, compared with TN, TNL showed an obvious absorption peak at 792 nm, indicating that IR780 was successfully loaded; TNIL had obvious absorption peaks at 792 nm and 299 nm, indicating the successful loading of IR780 and LND. In contrast, the absorption peak of TNILH was not obvious at 299 nm due to the increased absorption of HA from 250 nm to 350 nm. Fig. S6 (Supporting information) showed the variation of absorbance of IR780 and LND with concentration. Based on the UV-vis absorbance standard curve (Fig. S7 in Supporting information), the loading rates of IR780 and LND were 3.86% and 13.6%, respectively.

The degradation performance of TNILH in the simulated acidic tumor microenvironment and the applied ultrasound stimulation environment was further investigated. As shown in Fig. 1E, the release rates of IR780 in the acidic environment (pH 5.6) were both significantly higher than those in the neutral environment (pH 7.4) under the same experimental conditions, indicating that H^+ had a facilitating effect on the degradation of TNILH. Meanwhile, it was also found that the release of IR780 in different pH solutions was effectively improved after the addition of HAase, which proved the hydrolytic effect of HAase on the material surface. After comparison with the experimental group without HAase addition, the results illustrated that the HA-coated nanoformulation could reduce the premature release of IR780 in the circulation and reduce the toxic effects of the nanoformulations. In addition, when provided with ultrasound radiation assistance, the release rate of IR780 in acidic and neutral environments containing HAase could reach 65.48% and 34.70%, respectively, which was higher than the other experimental groups. It indicated that ultrasonic radiation could further accelerate the degradation of TNILH and facilitate the rapid release of IR780.

Next, we assessed the production of ROS during the acoustic dynamics by TNILH nanoformulation through the relative chemical probes (Fig. 1F). The production of $^1O_2$ and •OH were detected by electron spin resonance (ESR) spectroscopy. As shown in Fig. 1G, both the TiO_{2-x}@$NaGdF_4$@HA (TNH) and TiO_{2-x}@$NaGdF_4$@IR780@HA (TNIH) groups can produce •OH, and the TNIH group did not showed a stronger absorption peak, indicating that IR780 would not produce •OH under ultrasound radiation. Under the same conditions, the peaks of $^1O_2$ appeared in both the TNH and TNIH groups, and the intensity of the $^1O_2$ peak was stronger in the TNIH group (Fig. 1H). indicating that $^1O_2$ could be induced by ultrasound irradiation in both TN NPs and IR780.

In addition, 1,3-diphenylisobenzofuran (DPBF) was used as a fluorescent probe to detect ultrasound-induced ROS production [69,70]. The decomposition of DPBF exposed to the ultrasound environment was verified by UV-vis spectroscopy (Fig. S8 in Supporting information). After exposure to the ultrasound environment for 25 min, the absorption peaks of DPBF were hardly changed, demonstrating that DPBF can be stably present in the ultrasound environment. Then, the ultrasound-induced production of ROS by TNH and TNILH under different conditions was examined. As shown in Fig. S9 (Supporting information), both TNH and TNILH could produce ROS in PBS under ultrasound irradiation. Under the same pH conditions, TNILH exhibited more significant ROS generation efficiency than TNH, further demonstrating that IR780 could produce $^1O_2$ under ultrasound radiation, which could respond to the acidic conditions of the tumor microenvironment. The property was further confirmed by the decay curves of the absorption intensity of DPBF in different solutions (Fig. 1I).

Due to the excellent sonodynamic effect of TNIH nanoformulation, we further conducted the cellular experiment *in vitro* to evaluate the inhibitory effect on cancer cells. Fig. S10 (Supporting information) showed the schematic diagram of the killing mechanism of TNILH on cancer cells under ultrasound stimulation. Firstly, the phagocytic behavior of TNILH nanoformulation was investigated. As shown in Fig. S11A (Supporting information), blue fluorescence was derived from 4′,6-diamidino-2-phenylindole (DAPI) staining solution used to label the nucleus, and red fluorescence was derived from IR780 in TNILH. As the incubation time was extended, the red fluorescence in the HeLa cytoplasm was gradually brightening, indicating that TNILH nanoformulation had excellent tumor cell uptake, and the flow analysis data also proved the same result (Fig. S11B in Supporting information). It was due to the targeting effect of the HA coated with the material to the CD44 receptor on the surface of tumor cells.

Then, we systematically evaluated the biocompatibility of the materials by the typical standard methylthiazolyl tetrazolium assay (MTT). Specifically, we incubated L929 cells and HeLa cells with different concentrations of TNH, TNIH and TNILH (using Ti content as the calculated equivalent, Ti: 3.2, 6.4, 9.6, 12.8 and 16 ppm) and analyzed their cell viability. The results showed that all three nanoformulations (TNH, TNIH and TNILH) had no significant effect on cell viability without ultrasound stimulation (Figs. S12 and S13 in Supporting information), even at Ti concentrations up to 16 ppm. The viability of L929 cells treated by incubation with different materials was shown in Fig. 2A, indicating that the materials have good cytocompatibility for L929 cells. The viability of HeLa cells showed a clear trend of material concentration-dependent decrease after exposure to the ultrasound environment, and the survival rate of the HeLa cells treated with TNILH was only 21.15% when content concentration of Ti element was 16 ppm (Fig. 2B). It was attributed to the result of the SDT of TN and IR780 and the combined effect with LND.

Next, the effect of intracellular ROS production was evaluated with 2,7-dichlorofluorescein diacetate (DCFH-DA) as a probe for intracellular ROS detection. It can be seen that the fluorescence intensity of TNIH group was higher than that of TNH group when ultrasonic stimulation was applied (Fig. 2C), indicating a higher efficiency of ROS production in the presence of both TN NPs and IR780. Furthermore, HeLa cells treated with TNILH nanoformulation and ultrasound exhibited brighter green fluorescence, suggesting that the presence of LND could reduce the cellular oxygen consumption, which in turn could promote more ROS production (Fig. 2D). Meanwhile, in order to present more intuitive information about the killing effect of tumor cells in each group, we performed live-dead cell staining experiments (Fig. 2E). Compared with the TNH group, the TNIH group showed a significant cell death state under ultrasound radiation after loading IR780. The TNILH + US group showed nearly total cell death, visualizing the synergistic therapeutic effect between TN NPs, IR780 and LND.

Combined with the study of Fig. 1E, it was found that TNILH nanoformulation were able to release IR780 in an acidic environment. At the same time, it is also known that lysosome is the endpoint of cellular endocytosis, and the pH of its internal environment is about 4.0-5.0. Therefore, we speculated whether the nanoformulation would release IR780 through the lysosomal pathway and achieve the targeting of IR780 to mitochondria. So, we used Mito Tracker Green and Lyso Tracker Green to stain mitochondria and lysosome of HeLa cells for specific labeling to verify the cellular uptake behavior of TNILH and the mitochondrial targeting of IR780, respectively (Fig. 2F). After co-incubation with TNILH for 4 h, the red fluorescence of IR780 in HeLa cells overlapped with the green fluorescence of Mito Tracker Green, indicating that IR780 co-localized with mitochondria and that IR780 could accumulate in mitochondria. And at this time, the red fluorescence of IR780 also overlapped with the green fluorescence of Lyso Tracker Green, but both fluorescence intensities were significantly weaker. It was speculated that most of the materials have been decomposed in the lysosome and successfully “escaped” from

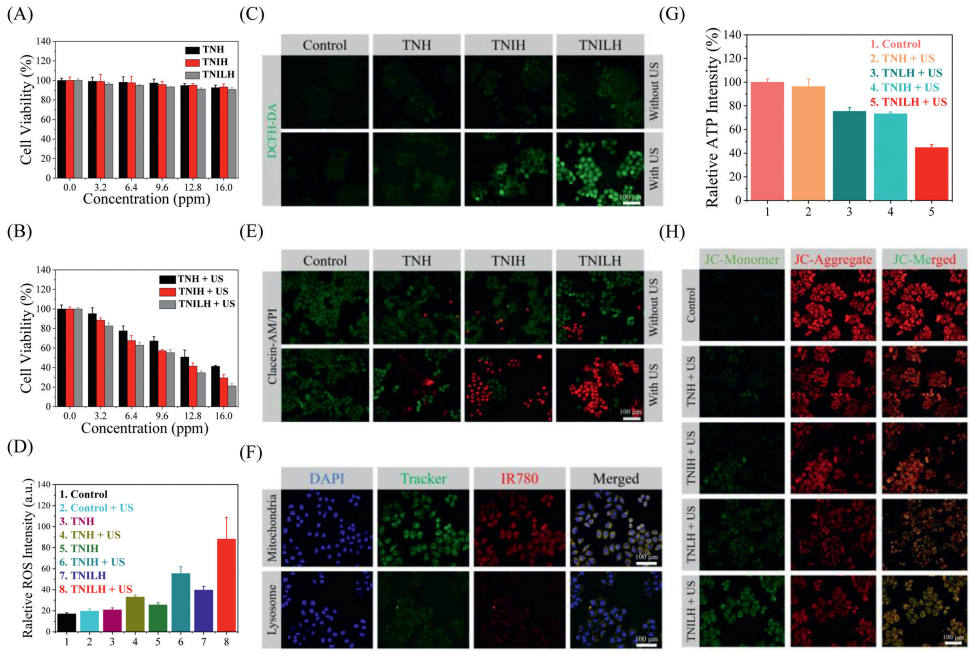

Fig. 2. *In vitro* cell apoptosis *via* the TNILH nanoformulation. (A) Viability of L929 cells after incubation with different concentrations of TNH, TNIH and TNILH. (B) Viability of HeLa cells incubated with different concentrations of TNH, TNIH and TNILH under ultrasound environment. (C) Fluorescence microscopy images of HeLa cells treated with DCFH-DA staining under different conditions. (D) Quantitative analysis of ROS generation in (C). (E) Fluorescence microscopy images of HeLa cells stained with PI (dead cells) and Calcein AM (live cells) after treatment with different conditions. (F) Fluorescence microscopy images of HeLa cells incubated with TNILH for 4 h, after treated with Mito-Tracker Green and Lyso-Tracker Green staining kits. (G) The control, TNH, TNLH, TNIH and TNILH group were incubated with HeLa cells for 6 h, and the content of ATP was detected after being stimulated by ultrasonic radiation. (H) Fluorescence microscopy images of mitochondrial membrane potential of HeLa cells stimulated by ultrasound radiation after 6 h of treatment with control, TNH, TNLH, TNIH and TNILH.

the lysosome under the test condition, and the released IR780 was successfully targeted into the mitochondria.

Then, we verified the effect of TNILH on mitochondrial function [50]. The effect of adenosine triphosphate (ATP) production in HeLa cells was detected by ATP assay kit. As shown in Fig. 2G, compared with the control group, the TNH + US group had little effect on the efficiency of ATP production. The TNILH + US group, which was loaded with both IR780 and LND, had the highest inhibitory effect on ATP, which was significantly better than the TNLH + US group loaded with LND alone and the TNIH + US group loaded with IR780 alone. It indicated that LND can effectively inhibit the activity of hexokinase II and reduce the production of the intracellular ATP. In the ultrasound environment, IR780 induced mitochondrial dysfunction by generating ROS, which synergized with LND to inhibit mitochondrial respiration. Afterwards, the effect of different treatment groups on mitochondrial membrane potential was verified by JC-1 assay kit (Fig. 2H). Similarly, the gradually enhanced green fluorescence was observed in the TNLH + US, TNIH + US and TNIL + US groups compared to the control and TNH + US groups, with the strongest green fluorescence intensity detected in TNILH + US group. It indicated that the synergistic effect of IR780 and LND would produce more significant disturbance of mitochondrial membrane potential in HeLa cells, thus disrupting mitochondrial function and inducing apoptosis more effectively.

Encouraged by the *in vitro* therapeutic effect, we then validated the *in vivo* therapeutic effect of TNILH [71–73]. At first, the effects of TNILH nanoformulation on the liver and kidney functions and hematological indices of mice were evaluated. Two groups of healthy mice ($n = 8$) were prepared, and TNILH (23.5 mg/kg) was injected through the tail vein into one group of mice as the experimental group, the same dose of PBS was injected into the other group of mice as the control group. Then, the blood biochemical indexes and hematological data of mice after the 14th day of injection were obtained separately (Fig. S14 in Supporting information). The experimental results showed that compared with the control group, no obvious changes were found in the blood indexes of the experimental mice after 14 days of intravenous injection of TNILH, indicating that the TNILH nanoformulation had no significant effect on the main blood indices.

Subsequently, the accumulation of TNILH at the tumor site was detected by MR imaging [74,75]. The existence of Gd elements conferred the ability of MR imaging of TNILH nanoformulation. We selected female BALB/c mice to establish a xenograft U14 tumor model. The TNILH was injected into the mice by tail vein injection. Subsequently, U14 tumor-bearing mice were scanned with a 3*T* clinical MR scanner equipped with special coils for mouse imaging, respectively, and imaging data were acquired at specific time points (0, 3, 6, 12, 24 and 36 h). As shown in Fig. S15A (Supporting information), the MR signal were detected at the tumor site as soon as 3 h after intravenous injection, and the strongest MR signal was detected at 12 h with increasing time. It indicated that TNILH had a good targeting effect and can be effectively accumulated at the tumor site. The MR imaging effect of different concentrations of TNILH nanoformulation *in vitro* was also detected by MR scanner, and the r_1 relaxation of TNILH nanoformulation was calculated to be 49.578 L mmol^{-1} ms^{-1} (Fig. S15B in Supporting information). In addition, the potential of TNILH for MR imaging was further demonstrated by comparing the bright and dark effects of tumor sites before and after *in situ* injection (Fig. S15C in Supporting information).

To examine the distribution and targeting effect of TNILH nanoformulation in mice [76,77], U14 tumor-bearing mice were injected with TNIL and TNILH nanoformulations, respectively. After the 6 h, 12 h, 24 h and 48 h intravenous injections, the content of Ti elements in the major organs (liver, heart, lung, spleen and kidney) and tumors of the mice were measured by ICP-MS (Figs. 3A and B). The results showed that the TNILH nanoformulation

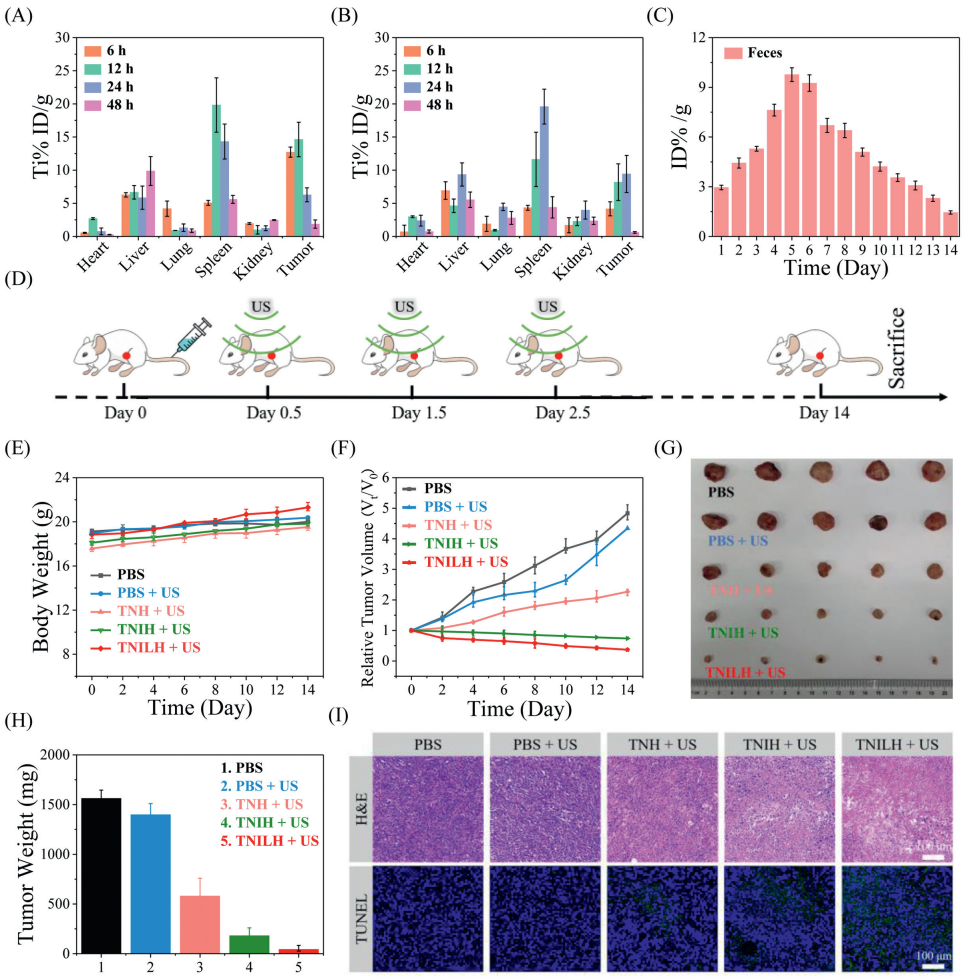

Fig. 3. *In vivo* antitumor effect of TNILH. (A) Biodistribution of Ti in major organs 6, 12, 24 and 48 h after intravenous TNILH injection. (B) Biodistribution of Ti in major organs after 6, 12, 24 and 48 h of intravenous TNIL administration. (C) Detection of TNILH in mouse feces within 1–14 days. (D) Schematic diagram of the treatment process of U14 tumor-bearing mice within 14 days. (E) Body weight change curve of mice treated with different ways over 14 days. (F) The change curve of tumor volume of mice treated with different ways over 14 days. (G) Photographs of tumors in mice treated by different treatment methods after 14 days of treatment. (H) Histogram changes of tumor weight of mice over 14 days under different treatments. (I) H&E and TUNEL staining images of tumor tissue treated with different methods.

would be captured by the reticuloendothelial system (liver and spleen) and excreted from the body mainly through the spleen. TNILH nanoformulation can accumulate rapidly at the tumor site at 6 h after intravenous injection and reach the maximum at 12 h. In contrast, the accumulation of TNIL nanoformulation at the tumor site only reached its maximum at 24 h. And the tumor sites of mice in the TNILH group could accumulate more nanoformulation than the TNIL group, proving the tumor-targeting effect of TNILH. In addition, we examined the feces of mice treated for two weeks by ICP-MS. As shown in Fig. 3C, the highest level of TNILH was found in the feces after 5 days of intravenous injection, achieving maximum clearance; within 14 days, nearly 75% of the nanoformulation was excreted through the feces. After 14 days of intravenous injection, only trace amounts of TNILH could be detected in the feces. It was an excellent proof that TNILH did not present long-term toxicity problems *in vivo*.

In the study of the *in vivo* tumor treatment effect of TNILH nanoformulation, we selected female BALB/c mice to establish a xenograft U14 tumor model and randomly divided 25 mice into 5 groups ($n = 5$): (A) PBS; (B) PBS + US; (C) TNH + US (20 mg/kg, based on Ti); (D) TNIH + US (20.8 mg/kg, based on Ti); (E) TNILH + US (23.5 mg/kg, based on Ti). After 0.5 days of intravenous injection (based on the optimal effect of MR imaging), (B), (C), (D) and (E) groups were subjected to one ultrasound treatment (1.0 MHz, 50% duty cycle, 1.5 W/cm^2, 5 min). The same treatment was done again on day 1.5 and day 2.5 (Fig. 3D). The change of weight and tumor volume of the mice were recorded every other day since the beginning of treatment until the end of treatment. Slight body weight fluctuations were found in all treatment groups, indicating that it was no significant adverse effect of the different treatments on the health of tumor-bearing mice (Fig. 3E). As shown in the change curve of tumor volume (Fig. 3F), tumor in the PBS and PBS + US groups grew rapidly, and the tumor growth was not inhibited. The TNH + US group indicated that the SDT effect produced by TN NPs had a certain inhibitory effect on tumor growth. Tumor growth was effectively inhibited in the TNIH + US and TNILH + US groups, and the best tumor inhibition was observed in the TNILH + US group, which proved the excellent synergistic therapeutic effect of the TNILH nanoformulation. The conclusion was further supported by digital photographs of tumors in mice (Fig. 3G) and histograms of tumor weight changes (Fig. 3H) at the end of treatment.

To further demonstrate the treatment effect, we performed H&E and TUNEL staining on the tumor tissue sections from different treatment groups [78–80]. As shown in Fig. 3I, comparing with other groups, H&E staining showed an obvious death or necrosis of tumor cells in the TNILH + US group, which was also confirmed by the TUNEL staining results. At the end of the treatment, we per-

formed H&E staining of the major organs (liver, heart, lung, spleen and kidney) of the mice (Fig. S16 in Supporting information). As it can be found, no significant damage to major organs was observed in the treated group compared to the PBS group, demonstrating that the treatment process was not significantly toxic to the organs.

In conclusion, we modified the ultrasmall TN NPs *via* the hydrophobic interaction of DSPE-PEG-NH_2 and adsorbed the sonosensitizing molecule IR780 by non-covalent bonding. Subsequently, LND and HA were loaded through amide bonds, and the multifunctional combined therapeutic nanoformulation TNILH was successfully synthesized. The effective accumulation of nanoformulation at tumor sites was achieved through the targeting effect of HA and IR780; dual acoustic sensitizers and small-molecule chemotherapeutic agents could achieve synergistic treatment. Due to the presence of Gd elements, TN NPs with asymmetric structures have MR imaging properties, which provide the possibility to realize real-time imaging of tumor sites of nanoformulation. In addition, both *in vivo* and *in vitro* data indicated that TNILH nanoformulation can effectively inhibit tumor growth with barely any side effects on normal tissues. More importantly, owing to the extremely small size, TNILH can be effectively excreted *in vitro* and does not cause long-term toxicity to mice. This work provided a new way for MR imaging-guided synergistic sonodynamic therapy and chemotherapy.

Data availability

The raw/processed data required to reproduce these findings are available from the authors.

Declaration of competing interest

The authors declare that they have no known competing financial interests or personal relationships that could have appeared to influence the work reported in this paper.

Acknowledgments

Z. F. Wang and M. Wang contributed equally to this work. This research was financially supported by the National Natural Science Foundation of China (Nos. 52250077, 52272156, 51872263 and 52202175), Taishan Scholars Project (No. ts20190911), Shandong Natural Science Foundation (No. ZR2020ZD36), and Guangdong Basic and Applied Basic Research Foundation (No. 2022A1515010461). All animal experiments were approved by the Center for Experimental Animals, Jilin University, Jilin, China, under production license number SCXK 2015-0001 and use license number SYXK 2018-0001. The procedures for the animal experiments were implemented under protocols of the National Regulation of China for Care and Use of Laboratory Animals. The authors would like to thank Xiaoju Li and Haiyan Sui from Shandong University Core Facilities for Life and Environmental Sciences for their help with the TEM.

Supplementary materials

Supplementary material associated with this article can be found, in the online version, at doi:10.1016/j.cclet.2022.107853.

References

[1] X. Wang, X. Zhong, L. Bai, et al., J. Am. Chem. Soc. 142 (2020) 6527–6537.
[2] X. Qian, Y. Zheng, Y. Chen, Adv. Mater. 28 (2016) 8097–8129.
[3] D. Li, Y. Yang, D. Li, et al., Small 17 (2021) 2101976.
[4] L. Sun, P. Wang, J. Zhang, et al., Biomater. Sci. 9 (2021) 1945–1960.
[5] H. Wang, J. Guo, W. Lin, et al., Adv. Mater. 34 (2022) 2110283.
[6] D.G. You, V.G. Deepagan, W. Um, et al., Sci. Rep. 6 (2016) 23200.
[7] D. Wang, D.B. Cheng, L. Ji, et al., Biomaterials 264 (2021) 120386.
[8] Y. Dong, S. Dong, B. Liu, et al., Adv. Mater. 33 (2021) 2106838.
[9] F. Gong, L. Cheng, N. Yang, et al., Adv. Mater. 31 (2019) 1900730.
[10] Q. Ren, N. Yu, L. Wang, et al., J. Colloid Interface Sci. 614 (2022) 147–159.
[11] Y. Lv, J. Zheng, Q. Zhou, et al., Sci. Rep. 7 (2017) 40967.
[12] X. Su, X. Wang, K. Zhang, et al., Gen. Physiol. Biophys. 33 (2014) 295–309.
[13] R. Zhang, L. Zhang, H. Ran, et al., Biomater. Sci. 8 (2020) 4581–4594.
[14] Z. Hou, Y. Zhang, K. Deng, et al., ACS Nano 9 (2015) 2584–2599.
[15] C. Dai, S. Zhang, Z. Liu, R. Wu, Y. Chen, ACS Nano 11 (2017) 9467–9480.
[16] X. Wang, X. Wang, X. Zhong, et al., Appl. Phys. Rev. 7 (2020) 041411.
[17] X. Han, J. Huang, X. Jing, et al., ACS Nano 12 (2018) 4545–4555.
[18] S. Liang, X. Deng, G. Xu, et al., Adv. Funct. Mater. 30 (2020) 1908598.
[19] Y. Cao, T. Wu, W. Dai, H. Dong, X. Zhang, Chem. Mater. 31 (2019) 9105–9114.
[20] S. Bai, N. Yang, X. Wang, et al., ACS Nano 14 (2020) 15119–15130.
[21] B. Geng, S. Xu, P. Li, et al., Small 18 (2022) 2103528.
[22] S. Zhang, S. Cao, T. Zhang, J.Y. Lee, Adv. Mater. 32 (2020) 2004686.
[23] B. Liang, B. Qiao, K. Yu, et al., ACS Appl. Mater. Interfaces 14 (2022) 13038–13055.
[24] J. Li, K. Kataoka, J. Am. Chem. Soc. 143 (2021) 538–559.
[25] M. Chang, Z. Hou, D. Jin, et al., Adv. Mater. 32 (2020) 2004647.
[26] T. Liu, Y. Chao, M. Gao, et al., Nano Res. 9 (2016) 3003–3017.
[27] X. Wei, Z. Feng, J. Huang, et al., ACS Appl. Mater. Interfaces 13 (2021) 32810–32822.
[28] Z.Y. Wang, Z.Y. Li, Z.L. Sun, et al., Sci. Adv. 6 (2020) eabc8733.
[29] P. Su, Z. Zhu, Q. Fan, et al., Inorg. Chem. Front. 5 (2018) 2620–2629.
[30] C. Qiao, X. Wang, G. Liu, et al., Adv. Funct. Mater. 32 (2021) 2107791.
[31] W.H. Chen, G.F. Luo, Q. Lei, et al., ACS Nano 11 (2017) 1419–1431.
[32] S. Chen, Q. Lei, W.X. Qiu, et al., Biomaterials 117 (2017) 92–104.
[33] Z. Luo, Y. Dai, H. Gao, Acta Pharm. Sin. B 9 (2019) 1099–1112.
[34] Q. Sun, Z. Kang, L. Xue, et al., J. Am. Chem. Soc. 137 (2015) 6000–6010.
[35] F. Zheng, C. Wang, T. Meng, et al., ACS Nano 13 (2019) 12577–12590.
[36] W.H. Chen, G.F. Luo, W.X. Qiu, et al., Biomaterials 117 (2017) 54–65.
[37] G. Huang, H. Huang, Drug Deliv. 25 (2018) 766–772.
[38] L.J. Hsu, M.F. Chiang, C.I. Sze, et al., Front. Cell Dev. Biol. 4 (2016) 141.
[39] K.Y. Choi, H.S. Han, E.S. Lee, et al., Adv. Mater. 31 (2019) e1803549.
[40] X. Zhang, Y. Wang, G. Wei, et al., J. Control. Release 322 (2020) 157–169.
[41] L. Jiang, S. Zhou, X. Zhang, et al., Nat. Commun. 12 (2021) 2390.
[42] L. Valcarcel-Jimenez, E. Gaude, V. Torrano, C. Frezza, A. Carracedo, Trends Endocrinol. Metab. 28 (2017) 748–757.
[43] Y.Q. Tan, X. Zhang, S. Zhang, et al., Biochim. Biophys. Acta Rev. Cancer 1876 (2021) 188534.
[44] V. Schirrmacher, Biomedicines 8 (2020) 526.
[45] M. Bordi, F. Nazio, S. Campello, Front. Oncol. 7 (2017) 81.
[46] H. Mei, X. Zhang, S. Cai, et al., Nano Today 41 (2021) 101305.
[47] S. Liu, W. Zhang, Q. Chen, et al., Nanoscale 13 (2021) 14049–14066.
[48] Y. Li, Q. Zhou, Z. Deng, et al., Sci. Rep. 6 (2016) 25968.
[49] J. Chen, H. Luo, Y. Liu, et al., ACS Nano 11 (2017) 12849–12862.
[50] C. Ji, J. Si, Y. Xu, et al., Theranostics 11 (2021) 8587–8604.
[51] H.B. Ruttala, T. Ramasamy, B.K. Poudel, et al., Acta Biomater. 101 (2020) 531–543.
[52] Y. Peng, J. Lu, R. Li, et al., ACS Appl. Mater. Interfaces 13 (2021) 26682–26693.
[53] J. Chen, F. Ren, W. Cao, et al., Nanomed. Nanotechnol. 34 (2021) 102370.
[54] L. Tang, X. Yang, Q. Yin, et al., Proc. Natl. Acad. Sci. U. S. A. 111 (2014) 15344–15349.
[55] K. Huang, H. Ma, J. Liu, et al., ACS Nano 6 (2012) 4483–4493.
[56] T.J. Liu, X. Zhang, D.Z. Liu, et al., Adv. Opt. Mater. 9 (2021) 2100233.
[57] Y. Han, H. Liu, M. Fan, et al., J. Colloid Interface Sci. 616 (2022) 595–604.
[58] D. Shao, J. Li, X. Zheng, et al., Biomaterials 100 (2016) 118–133.
[59] Q. Wu, Y. Lin, F. Wo, et al., Small 13 (2017) 1701129.
[60] S. Liang, X. Deng, Y. Chang, et al., Nano Lett. 19 (2019) 4134–4145.
[61] Z. Wang, F. Zhang, D. Shao, et al., Adv. Sci. 6 (2019) 1901690.
[62] L. Zeng, Y. Pan, Y. Tian, et al., Biomaterials 57 (2015) 93–106.
[63] Z. Wang, B. Liu, Q. Sun, et al., ACS Nano 15 (2021) 12342–12357.
[64] H. Li, D. Luo, C. Yuan, et al., J. Am. Chem. Soc. 143 (2021) 17097–17108.
[65] R. Zhang, Q. Zeng, X. Li, D. Xing, T. Zhang, Biomaterials 275 (2021) 120993.
[66] X. Chen, H. Zhou, X. Li, et al., EBioMedicine 30 (2018) 129–137.
[67] C. Zhao, L. Shao, J. Lu, et al., ACS Appl. Mater. Interfaces 9 (2017) 18450–18461.
[68] P.E. Saw, J. Park, E. Lee, et al., Theranostics 5 (2015) 746–754.
[69] H. Bi, Y. Dai, P. Yang, et al., Small 14 (2018) 1703809.
[70] Q. Cai, D. Yang, L. Zhong, P. Yang, Chem. Mater. 32 (2020) 7492–7506.
[71] H. Wang, W. Yang, K. Bian, et al., Small 18 (2021) 2104550.
[72] X. Zheng, W. Liu, J. Ge, et al., ACS Appl. Mater. Interfaces 11 (2019) 18178–18185.
[73] M. Wang, M. Chang, Q. Chen, et al., Biomaterials 252 (2020) 120093.
[74] J. Zhang, Y. Yin, J. Zhang, et al., Nano Lett. 22 (2022) 2514–2520.
[75] Q. Sun, F. He, C. Sun, et al., ACS Appl. Mater. Interfaces 10 (2018) 33901–33912.
[76] M. Wang, M. Chang, C. Li, et al., Adv. Mater. 34 (2022) 2106010.
[77] N. Tao, H. Li, L. Deng, et al., ACS Nano 16 (2021) 485–501.
[78] Z. Zheng, Z. Jia, C. Qu, et al., Small 17 (2021) 2006508.
[79] Y. Liu, M. Jiang, Y. Tu, et al., Biomaterials 278 (2021) 121136.
[80] X. Wang, Y. Zhao, Y. Hu, et al., Small 17 (2021) 2102269.